Breakup threshold anomaly in the elastic scattering for the ^{6}Li + ^{90}Zr system

H. Kumawat,* V. Jha,† B. J. Roy, V. V. Parkar, S. Santra, V. Kumar, D. Dutta, P. Shukla, L. M. Pant, A. K. Mohanty, R. K. Choudhury, and S. Kailas
Nuclear Physics Division, BARC, Mumbai 400085, India
(Received 13 August 2008; published 27 October 2008)

Measurements of elastic scattering for the ^{6}Li + ^{90}Zr system has been performed at various energies, namely, 11, 12, 13, 15, 17, 19, 21, 25, and 30 MeV, to study the energy dependence of the interaction potential. Angular distributions have been measured in a wide angular range to extract the behavior of the potential reliably. The data have been analyzed using the phenomenological Woods-Saxon shaped optical potential and the double folding potential. The potential behavior shows the characteristics of the breakup threshold anomaly, namely, the increase in the imaginary potential near the barrier with a small reduction in the real part. Continuum-discretized-coupled-channel (CDCC) calculations give a good description of the measured elastic scattering data and predict large breakup coupling effects. The polarization potentials extracted from the CDCC calculations have been studied for the present system along with those for the ^{6}Li + ^{208}Pb, and ^{6}Li + ^{28}Si systems, and a similar energy dependence has been obtained for all the cases considered.

DOI: 10.1103/PhysRevC.78.044617 PACS number(s): 25.70.Bc, 25.70.Mn

I. INTRODUCTION

The existence of the threshold anomaly (TA) in the interaction potential describing the elastic scattering between heavy ions at energies around the Coulomb barrier has been well established for tightly bound nuclei [1]. The anomaly refers to an observation of a localized peak in the real part of the potential (usually assumed as an optical potential or a double folding potential) in the vicinity of the Coulomb barrier associated with a sharp fall in the imaginary part of the interacting potential in the same energy region. The origin of this effect has been understood in terms of an attractive polarization potential generated due to inelastic couplings in both the target and the projectile and to the transfer channels. It has been shown that the relation between the real and the imaginary parts of the interacting potential is due to causality and consequently obeys the dispersion relations. At higher energies, however, the real and the imaginary parts of the optical potential are expected to be energy independent.

A subject of increasing interest in recent years is the investigation of the influence of the breakup channel on the other reaction channels when weakly bound projectiles are involved. It has been found that the coupling to breakup channels introduces a repulsive real polarization potential [2] and only a weak imaginary potential at all energies. It has been shown that this feature might lead to the washing out of the conventional threshold anomaly resulting in no energy dependence of the potential even at near barrier energies. More recently, based on analysis of experimental data, it has been suggested that the potential for the imaginary part may have an increasing trend associated with a small reduction in the real part of the potential near the barrier. This new feature was termed the breakup threshold anomaly (BTA) and an attempt has been made to understand it by dispersion relations [3,4]. The explanation of this phenomenon is given in terms of continued and probably increased relative importance of the breakup channel at energies in the vicinity of the barrier, which leads to a shift in the threshold to even lower energies. Several works have been devoted to studies of elastic scattering in the vicinity of the Coulomb barrier for weakly bound stable nuclei [5–13] in recent times. However, there exists contradictory conclusions regarding the presence of TA or BTA for the behavior of potential describing elastic scattering of weakly bound projectile nuclei on different targets. The BTA phenomena has been seen more clearly in the ^{6}Li + ^{208}Pb [5] system and to some extent in the ^{6}Li + ^{138}Ba [7] and ^{6}Li + ^{58,64}Ni [14] systems, while it is not clear from measurements for many other systems [8,11,13,15]. Extraction of the correct behavior of the potential is difficult, as the BTA should appear at energies close to or below the barrier where the Coulomb potential is the dominating part of the interaction potential. The effect of the nuclear potential is seen only at very large angles as one approaches the barrier. Therefore, good quality data at lower energies, especially at backward angles, are required to extract the interaction potential reliably.

Elastic scattering of the weakly bound nuclei with targets of different mass ranges can show different potential behaviors due to the varying importance of the nuclear and Coulomb breakup apart from specific effects due to couplings to the other channels such as target inelastic excitations and transfer. The measurements for light mass nuclei were prompted because of the fact that light mass nuclei should be free from the large Coulomb domination expected for the heavy nuclei [8,16]. In the present work, we have performed measurements of elastic scattering angular distributions for medium mass nuclei using the ^{6}Li + ^{90}Zr system. Measurements have been performed at a range of energies from the relatively deep subbarrier energies to above barrier energies (30 MeV) to map the behavior of the interaction potential around the barrier. The target ^{90}Zr nucleus is a spherical neutron magic nucleus and

*Corresponding author: harphool@barc.gov.in
†Present address: IKP, Forschungszentrum, Jüelich D-52425, Germany; v.jha@fz-juelich.de

it is expected that the collective excitations of the target do not play an important role. Dominant contributions from only couplings to breakup and transfer channels are expected. A systematic analysis of the effect of breakup couplings via the optical model approach and the continuum-discretized-coupled-channel (CDCC) approach has been made. We have also performed comparisons for different mass systems to study the effect of breakup for different target mass ranges using the CDCC framework.

The outline of this article is as follows. In Sec. II we present experimental details and the measurements. Section III contains the analysis in the phenomenological optical model framework. In Sec. IV, a folding model analysis is presented. In Sec. V, the analysis of dispersion calculation for the energy dependent behavior of the potential is given. In Sec. VI continuum-discretized-coupled-channel (CDCC) calculations for study of the breakup effect of the $^{6}\mathrm{Li} + {}^{90}\mathrm{Zr}$ system are presented. Section VII considers a study of the target mass dependence for the study of the breakup polarization potential. Conclusions are given in Sec. VIII.

II. EXPERIMENTAL DETAILS

Experimental measurements were performed using the $^{6}\mathrm{Li}^{3+}$ beam delivered by the 14UD Pelletron accelerator of the TIFR/BARC Facility in Mumbai, India, at bombarding energies 11, 12, 13, 15, 17, 21, 25, and 30 MeV. The beam energies were corrected for the half target thickness in the analysis process that amounts to a minimum of 71.2 keV for 30 MeV and a maximum of 132.6 keV for 11 MeV. Beam currents were typically in the range of 5–30 nA. The current was measured using a Current Integrator, the output of which was fed into a CAMAC Scaler to obtain the integrated charge. The beam impinged on a 400 μg/cm^2, self-supported enriched ^{90}Zr ($\geqslant$99%) target and the elastically scattered ^{6}Li ions were detected by four solid state silicon surface barrier detectors in a $\Delta E + E$ telescopic arrangement. The telescopes were constituted with different thicknesses, namely, T_1 with $\Delta E =$ 27 μm and $E =$ 1000 mm thick, T_2 with $\Delta E =$ 21.4 μm and $E =$ 1000 mm thick, T_3 with $\Delta E =$ 17 μm and $E =$ 521 mm thick, and T_4 with $\Delta E =$ 50 μm and $E =$ 2000 mm thick. The telescopes were placed on a rotatable arm inside a 1 meter scattering chamber at angular separation of 10° between each telescope. The solid angles subtended by the telescopes at the target center were 0.28, 0.28, 0.36, and 0.28 msr, respectively. The angular opening corresponding to these solid angle values were in the range of 0.5° to 0.8°. A monitor detector of thickness 1000 mm was also mounted at a forward angle for absolute normalization. The relative normalization between the telescopes was determined from the measurements at various overlap angles at which the data were acquired. Angular distributions were measured at angles from 25° to 173° at lower energies and from 25° to 100° at higher energies. The statistical error in the data was less than 1% in the forward angles and a maximum of 2% at the backward angles. The data were recorded using the Linux based data acquisition system LAMPS [17].

III. PHENOMENOLOGICAL CALCULATIONS

An optical model analysis of the elastic scattering differential cross section was performed using FRESCO code [18]. This code has recently incorporated the well-known multiparameter search program MINUIT. The volume Woods-Saxon form was used for both the real and the imaginary part of the optical potential. The starting parameters for the search were taken from Ref. [19] and used in the analysis of 34 MeV elastic scattering data of $^{6}\mathrm{Li} + {}^{90}\mathrm{Zr}$. Searches were carried out by varying all six parameters (strength, radius, and diffuseness of real and imaginary potentials) simultaneously as well as an independent search for each parameter fixing all others and also with different combinations of the parameters, to achieve a best fit to the data. The best fit parameters obtained at various energies and the corresponding reaction cross sections are given in Table I. The fits with the elastic scattering data are given in Figs. 1 and 2. It is important to note that the deviation from Rutherford scattering occurs at very large angles as one approaches the barrier and there is a singular lack of data at these backward angles in most of the earlier data. We have measured up to 173° at various energies near and far below the barrier which is necessary to extract information about the nuclear potential.

To probe the energy dependence of the potential in the vicinity of the barrier, it is important to find out the radius of sensitivity (crossing radius) where the potential can be best determined by the elastic scattering data. We have varied the diffuseness parameter near the best fit value and found the equivalent fits of the elastic scattering data within the range for which $\chi^2 = \chi^2_{\min} \pm \chi^2_{\min}/2$ [20]. The crossing of the potentials, derived from the equivalent fit to the experimental data, at a value of the radius termed the crossing radius ensures that the crossing radius is the sensitivity radius. Both imaginary and real radii were found to be energy dependent and the dependence vanishes with the increase in energy. The average radius was estimated to be 10.5 ± 0.6 fm ($R_r = 9.9$ fm for the real part and $R_i = 11.1$ fm for the imaginary part). The crossing radii for both the real and imaginary parts at 20.91 MeV are shown in Fig. 3. The potentials were estimated at this radius to determine their energy dependent behavior. The energy dependence of the real and imaginary potentials

TABLE I. The best fit optical potential parameters from elastic scattering data where the radius is given by $R_{0,w} = r_{0,w}(A_1^{1/3} + A_2^{1/3})$ and N represents the number of data points.

E_{lab} (MeV)	V_0 (MeV)	r_0 (fm)	a_0 (fm)	W_0 (MeV)	r_w (fm)	a_w (fm)	χ^2/N	σ_R (mb)
10.87	42.6	1.129	1.158	44.4	1.084	0.786	1.155	0.34
11.87	42.7	1.129	1.217	44.3	1.084	0.851	0.134	3.6
12.88	42.6	1.129	1.054	44.4	1.084	0.920	0.751	20.5
14.89	42.6	1.213	0.642	44.5	1.147	0.740	0.354	41.6
16.90	42.6	1.124	0.694	44.4	1.097	0.790	0.585	175.3
18.90	41.7	1.126	0.660	44.2	1.054	0.834	0.377	404.7
20.91	44.9	1.133	0.679	44.3	1.143	0.715	1.687	647.5
24.92	43.2	1.128	0.660	52.0	1.039	0.835	1.017	1085.8
29.93	43.5	1.130	0.665	46.7	1.082	0.837	0.048	1508.9

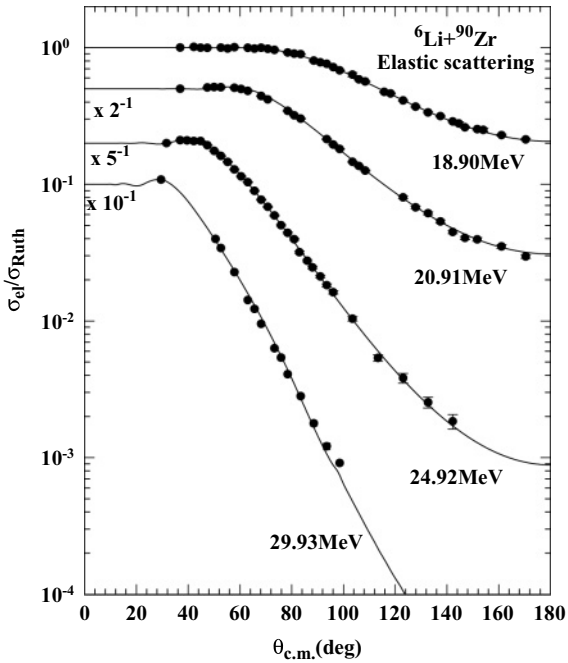

FIG. 1. Elastic scattering data for the $^6\mathrm{Li} + {}^{90}\mathrm{Zr}$ system above the Coulomb barrier. The Coulomb barrier is taken as 18.1 MeV in the laboratory frame for this system. The statistical errors in the data are less than 2%. The lines show the phenomenological model fit to the data. The best fit parameters are given in Table I.

calculated at the sensitivity (crossing) radius is plotted in Fig. 4 where the total potential is given as $V + iW$. The real part of the potential remains nearly constant until the barrier is reached with a slight dip around the barrier and further increases at still lower energies. As for the imaginary part, an uprising trend

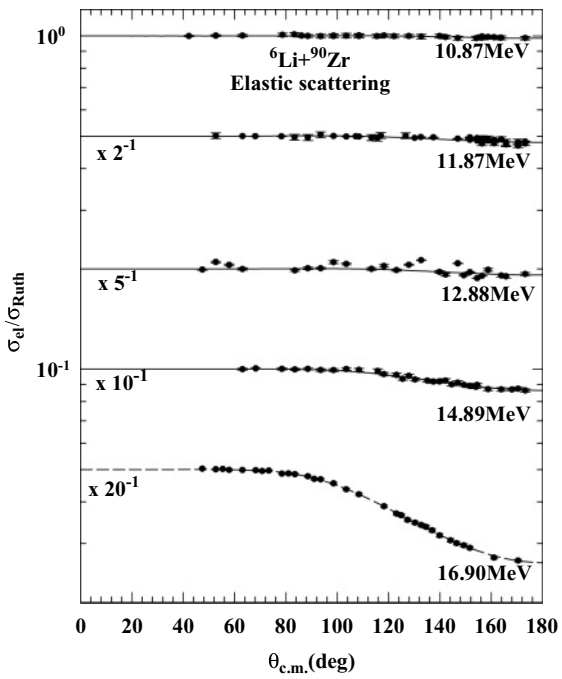

FIG. 2. Same as Fig. 1.

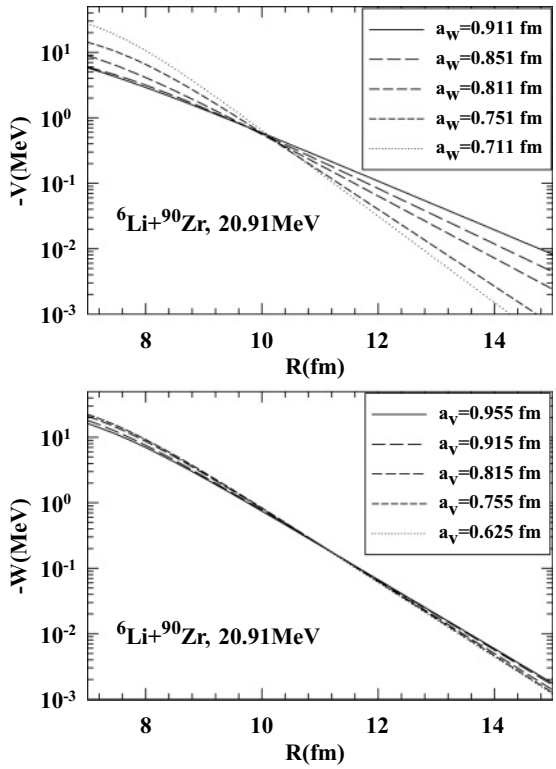

FIG. 3. The crossing radius obtained for the $^6\mathrm{Li} + {}^{90}\mathrm{Zr}$ system with the best fit optical potential at 20.91 MeV.

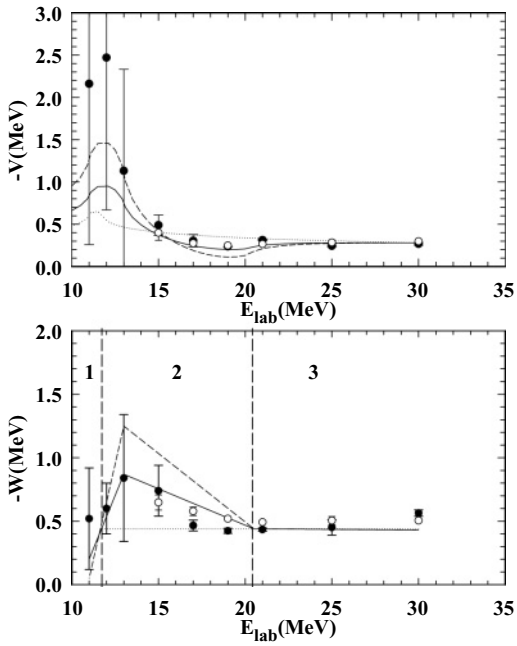

FIG. 4. Real and imaginary parts of the optical potentials at $R = 10.5$ fm, obtained with the best fit phenomenological model (solid circle) and the double folding model (open circle). The dispersion analysis was performed with three segmented imaginary parts with three different slopes and the resulting calculated real parts are shown by lines. Three different slopes were considered, taking into account the errors in the experimental data.

is observed around the barrier and it finally decreases toward zero.

IV. THEORETICAL ANALYSIS: DOUBLE FOLDING FRAMEWORK

Following the optical model analysis, the elastic scattering data were analyzed in the double folding framework [21] with folded M3Y potential [21]. The double folded potential can be calculated as

$$V_F = \int\int d\mathbf{r}_1 d\mathbf{r}_2 \rho(\mathbf{r}_1)\rho(\mathbf{r}_2)v(\mathbf{r}_{12}), \quad (1)$$

where $\mathbf{r}$ is the separation between the centers of the two colliding nuclei, v is the effective nucleon-nucleon interaction potential, and ρ_1 and ρ_2 are the point nucleon densities of ^{6}Li and ^{90}Zr. The potentials were computed using the code DFPOT [22]. The densities for ^{6}Li are computed from parameterized charge distributions taken from Ref. [23] and a three-parameter Gaussian distribution [24] is used to get the density for ^{90}Zr. The point charge distribution was obtained after correcting for finite size of the proton [21] using root mean square radii, 2.56 and 4.28 fm for ^{6}Li and ^{90}Zr, respectively. The imaginary part of the folding potential was identical to that of the real part of the folding potential. Thus the total potential considered was of the form

$$U(r) = V_c(r) - \lambda_r V_F(r) - \lambda_w V_F(r). \quad (2)$$

To start with we have calculated the elastic angular distributions with the potential without any renormalization (The normalization constants N_R and N_I were fixed to unity).

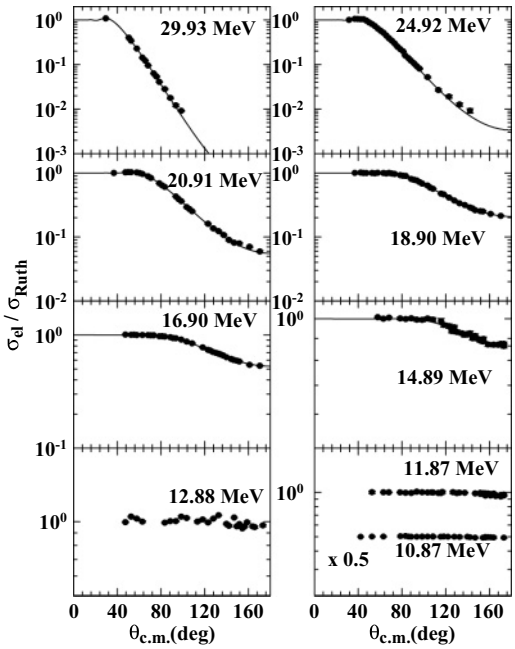

FIG. 5. Results of the double folding model analysis to fit to the elastic scattering data above barrier for the ^{6}Li + ^{90}Zr system. The best fit parameters are given in Table II.

TABLE II. The real and imaginary parts of the potential were assumed to be the same and were calculated using the double folding model with two different normalization factors, N_R and N_I, for the real and imaginary parts, respectively. The values of N_R and N_I are given for the best fit to the elastic scattering data.

E_{lab} (MeV)	N_I	N_R	χ^2/N	σ_R (mb) (DF)	σ_R (mb) (CDCC)
10.87					0.39
11.87					3.50
12.88					8.3
14.89	1.41	0.87	0.342	69.4	47.0
16.90	1.26	0.58	0.693	200.4	170.7
18.90	1.13	0.54	1.120	412.7	416.9
20.91	1.07	0.57	1.7	676.3	664.8
24.92	1.10	0.61	1.015	1083.3	1062.1
29.93	1.11	0.62	0.048	1494.9	1398.2

Subsequently, the values of N_R and N_I were varied as free parameters to obtain a best fit to the data. The derivation of the error bars was similar to that performed for the phenomenological optical model fits. The deduced angular distributions are given in Fig. 5. The real and imaginary parts of the potential at $R = 10.5$ fm are given in Fig. 4 and a good agreement between the phenomenological and microscopic potentials is observed. The parameters along with the reaction cross-section values corresponding to the best fit of the elastic scattering data are given in Table II. The value of $N_R = 0.6$ is obtained at higher energies and it is marginally reduced around the Coulomb barrier. It shows that an overall repulsive polarization potential is generated by the couplings that compensates the attractive behavior expected for the stable nuclei. This finding of repulsive polarization potential corroborates that observed from the phenomenological fit given in Sec. III. As we have seen in the phenomenological calculations/fits, one requires a higher diffuseness parameter to fit the data at deep subbarrier energies. The double folding model allows one to vary only the strengths of the real and imaginary parts of the potential to fit the data, not the geometry. If one attempts to fit the data by varying N_R and N_I only, these values turn out to be unphysical ($N_R = 80$, $N_I = 4$ at 10.87 MeV); so we have omitted fits at deep subbarrier energies.

V. DISPERSION CALCULATIONS

The energy dependence of the optical potential near the barrier shows consistent behavior in the optical model and double folding framework and it can be tested using dispersion relations [2]. The elastic scattering cross section can be reproduced by introducing an effective interaction/optical potential that accounts for all coupling effects and thus the many-body problem can be reduced to a one-body problem with an equivalent potential.

$$U(r, E) = V(r, E) + iW(r, E), \quad (3)$$

where V and W are the real and imaginary parts of the potential and are connected through the dispersion relation:

$$V(r, E) = V_0(r, E) + \Delta V(r, E),$$
$$\Delta V(r, E) = \frac{P}{\pi} \int_0^\infty \frac{W(r, E')}{E' - E} dE', \quad (4)$$

where ΔV is an attractive polarization potential. The imaginary potential W has little effect on ΔV at low energy; therefore V_0 can be normalized at some energy E_s,

$$V(r, E) = V_0(r, E_s) + \frac{P}{\pi}(E - E_s) \times \int_0^\infty \frac{W(r, E')}{(E' - E_s)(E' - E)} dE'. \quad (5)$$

We have used the linear segment model proposed in Ref. [2] for $W(r, E)$ and tried to get the real part. These dispersion relations for phenomenological and folding models are given in Figs. 4 and 6, respectively. Three different slopes were chosen considering the errors in the deduced experimental imaginary potential (normalization factor in the case of Fig. 6). It is clear from Figs. 4 and 6 that the upper two slopes of the imaginary potential used in the dispersion relation could reproduce the real counterpart in better proximity with deduced experimental data. The presence of breakup even at relatively lower energies around the barrier doesn't allow the imaginary potential to vanish. In fact the imaginary potential is increasing as one approaches the barrier. This leads to an associated reduction in the real potential at energies near the barrier. Ultimately, however, the imaginary potential vanishes due to the closure of the breakup channel at energies well below the barrier. The real part of the potential shows increasing behavior below the barrier where the imaginary part falls down. The reaction threshold for the closure of channels is found to have shifted to lower energies. It is clear that analysis in the folding model and optical model framework shows the presence of a breakup threshold anomaly (BTA) for this system that is reasonably well explained by the dispersion calculations.

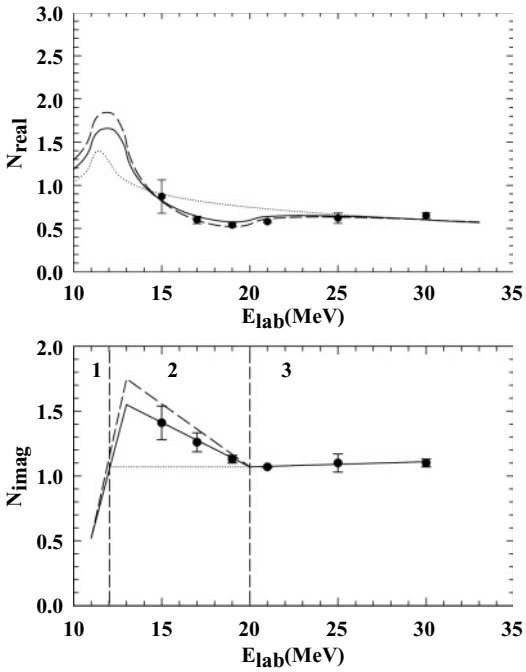

FIG. 6. Real and imaginary normalization factors for the double folded potential. The dispersion analysis was performed with three segmented imaginary parts with three different slopes and the resulting calculated real part are shown by continuous lines. Three different slopes were considered taking into account the errors in the experimental data.

We divided the imaginary part of the potential into three different energy regions, namely, (1) deep subbarrier, (2) around the Coulomb barrier, and (3) well above the barrier, to understand the effect of the BTA on the polarization potential. Three different shapes were considered for the dispersion calculations. In one case, the shape of the imaginary potential is seen to be similar (dotted lines in Figs. 4 and 6) to that of the potential for strongly bound stable nuclei where it increases first and then gets saturated. The TA present in the case of strongly bound stable nuclei seems to exist at deep subbarrier energies where breakup effects are expected to be negligible. The imaginary part of the potential first increases at deep subbarrier energies, then decreases around the barrier, and further gets saturated well above the barrier in the case of the weakly bound nuclei. The increase in the imaginary part of the potential around the barrier is in contrast to that observed for the strongly bound nuclei. This increase resulted in a dip in the real potential around the barrier that was absent in the case of the strongly bound ones and it is because of the repulsive polarization potential due to breakup coupling effects. This dip may shift below or above the barrier for heavy or light targets as shown later in Sec. VII. Kailas [25] has also shown that the real normalization (N_{real}) values go up from 0.6 to 1.0 because of the TA.

VI. THEORETICAL ANALYSIS: CDCC CALCULATIONS

To study the breakup coupling effects for ^{6}Li detailed CDCC calculations have been performed using the the code FRESCO, version FRXY.li [18,26]. The ^{6}Li nucleus is assumed to have a two body $\alpha + d$ cluster structure. The continuum above the $^6\text{Li} \longrightarrow \alpha + d$ breakup threshold (1.47 MeV) was discretized into momentum bins of widths $\Delta k = 0.2$ fm^{-1}. The continuum states with relative orbital angular momentum $L = 0, 1, 2$, and 3 were included in the calculations. In addition, the 1^+, 2^+, and 3^+ resonances for $L = 2$ were also included in the calculations. To include these resonances in the coupling scheme the continuum bin widths were suitably modified to avoid any double counting due to their inclusion. The continuum momentum bins were truncated at the upper limits of $k_{\max} = 1.2$ fm^{-1} (corresponding to $\epsilon_{\max} = 14.23$ MeV) for calculations at $E_{\text{lab}} = 30$ MeV and were reduced with a decrease in energy to a value $k_{\max} = 0.7$ fm^{-1}($\epsilon_{\max} = 5.516$ MeV) at 15 MeV. The binding potentials between the α-d clusters used to calculate the bin wave functions were taken from Ref. [27].

The CDCC calculations require the $\alpha + {}^{90}$Zr and the $d + {}^{90}$Zr optical potentials as an input to generate the potential for

the ^{6}Li + ^{90}Zr potential by the single folding technique. These potentials were obtained from global $\alpha + {}^{90}$Zr [28] and $d + {}^{90}$Zr [29] optical model potentials. The real part of the global potential strength for the $\alpha + {}^{90}$Zr system was renormalized by a factor of 0.45, which was necessary to fit the values in the Coulomb rainbow region of higher energy data (34 MeV data [19] are available from the literature). The subsequent calculations were performed using the same potential without any further adjustment. The potential used for $d + {}^{90}$Zr is the unmodified potential from Ref. [29].

The results of the CDCC calculations are shown in Fig. 7 along with the measured data. The dashed and solid curves show the calculations with and without the inclusion of the breakup couplings. As can be seen a very good description of the elastic scattering data is obtained by the CDCC calculations at all energies. A large effect due to the breakup coupling effects is visible in the elastic scattering cross section at energies above the barrier and it reduces gradually as the barrier is approached.

The effect of breakup couplings may be directly understood in terms of the dynamical polarization potential (DPP). The DPP generated due to the breakup couplings added to the bare potential can simulate the breakup in one channel calculations. The real and imaginary parts of the polarization potentials generated by the breakup couplings have been generated in the calculations with the prescription of Thompson *et al.* [30]. These potentials, around and above the sensitivity radius, at various energies are plotted in Fig. 8. As can be seen, the derived polarization potentials from the breakup couplings give rise to a large repulsive real potential and a small imaginary potential. The increase of the backward angle elastic cross section with respect to the calculations without breakup couplings shown in Fig. 7 is consistent with the repulsive real polarization potential generated by the breakup couplings. The couplings also generate a small absorptive potential as seen by the slight reduction in cross section at the relatively forward angles for higher energies.

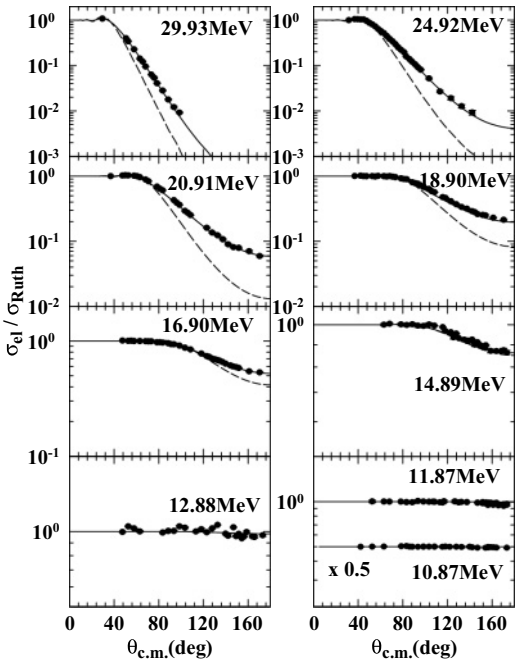

FIG. 7. CDCC analysis of the elastic scattering data. Dashed lines represent the CDCC calculations without breakup coupling and the solid lines represent the CDCC calculations with breakup coupling.

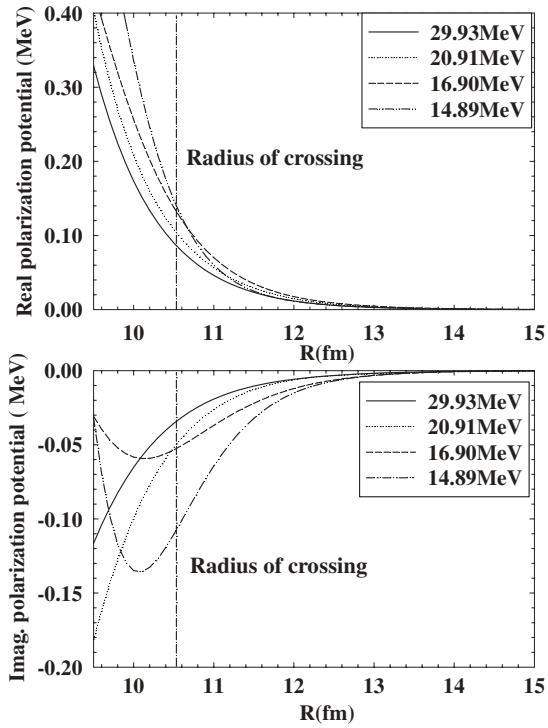

FIG. 8. Real and imaginary breakup polarization potentials generated by CDCC calculations at 29.93, 20.91, 16.90, and 14.89 MeV energies.

The projectile breakup effects in elastic scattering of ^{6}Li have been investigated extensively by Sakuragi [31] in the CDCC framework for a wide range of incident energy and mass ($E_{\rm lab} = 40$–170 MeV and $A = 12$–208), which are in general higher than the present case. In that work, ^{6}Li-target interactions were obtained using the double folding potential. The calculations could reproduce the experimental data of elastic scattering for all the targets and incident energies investigated, without any renormalization of the folding real potential. The breakup effect was found to independent of target and energy. It was shown that the calculated results are quite sensitive to the strength of the imaginary coupling potentials, and $N_I \simeq 0.5$–0.6 was required for a reasonable agreement with the experimental data. In contrast to Ref. [31], we have adopted the cluster folding approach to generate ^{6}Li-target interaction potentials that are also independent of energy. We also performed the calculations with different renormalization values for the imaginary part of the interaction potentials. However, it was not possible to fit the data with the smaller strength of the imaginary potentials. As in Ref. [31], it was found that the higher values of the imaginary potential generate a more repulsive real polarization potential that helps to fit the data.

VII. COMPARISONS WITH OTHER SYSTEMS

It is important to investigate the coupling effects of the breakup channel on the elastic scattering cross sections for various target nuclei having different masses. It is expected that the interaction of the weakly bound nuclei with heavy nuclei will be dominated by the large Coulomb breakup contribution. In contrast, the nuclear breakup will have a greater role in the interaction with the relatively lighter nuclei. We have considered two other systems (^{6}Li + ^{208}Pb and ^{6}Li + ^{28}Si) apart from the ^{6}Li + ^{90}Zr system as representatives for heavy and light target mass nuclei, respectively. CDCC calculations have been performed at a range of energies to study the role of breakup on the interaction potential for these systems. For calculations, the global potentials for $\alpha, d + ^{208}$Pb and $\alpha, d + ^{28}$Si were taken from the same reference as that for $\alpha, d + ^{90}$Zr [28,29]. The α potentials were renormalized to fit the available high energy data (^{6}Li + ^{208}Pb [5] and ^{6}Li + ^{28}Si [8]). For the $\alpha + ^{208}$Pb potential, the real part was renormalized by a factor of 0.7 while the imaginary part was taken without any normalization. For $\alpha + ^{28}$Si, the real strength was normalized by 0.45 and the imaginary potential normalized by a factor of 0.6. The calculations for the lower energies were performed by the same potential. The polarization potentials for the ^{6}Li + ^{208}Pb and ^{6}Li + ^{28}Si systems were derived at the respective radii which were calculated after scaling according to $R = (A_P^{1/3} + A_T^{1/3})$ from the one that was obtained for the ^{6}Li + ^{90}Zr system. The real and imaginary parts of the polarization potentials generated with the full (nuclear+Coulomb) and nuclear breakup coupling calculations are shown in Fig. 9, as evaluated at the radii of sensitivity for these three systems. The imaginary polarization potential increases associated with a decrease in the repulsive real polarization potential for the energies around the barrier for each case. Further, from the shape of energy dependence of the polarization potentials in Fig. 9, one can conclude that the increase in the repulsive real polarization potential (increase of the absorptive imaginary polarization potential) is seen at lower $E_{\text{c.m.}}/V_B$ for the heavy targets ($E_{\text{c.m.}}/V_B = 0.8$ for ^{6}Li + ^{208}Pb) as compared to the light targets ($E_{\text{c.m.}}/V_B = 1.2$ for ^{6}Li + ^{58}Si). The calculations were performed separately for pure Coulomb and nuclear coupling potentials. However, the pure nuclear coupling effect was found to be the dominating component for all the mass systems studied and it gives almost an equivalent fit to elastic cross sections as the total couplings. The polarization potentials generated by the Coulomb couplings have a behavior opposite to that generated because of the nuclear couplings. Further, the polarization potential due to the Coulomb part (extracted after subtracting the polarization potential due to the nuclear couplings from the total polarization potential) contributes only 10, 15, and 20% to the total breakup polarization potential in the ^{6}Li + ^{28}Si,^{6} Li + ^{90}Zr, and ^{6}Li + ^{208}Pb systems respectively. Thus the total breakup polarization potential arises mainly because of the nuclear couplings in all the three systems considered. This dominance of the nuclear coupling effects leads to a total interaction potential that shows an energy dependence with an overall increase in the imaginary part and an associated decrease in the real part (due to more repulsive polarization potential) around the barrier. Thus, the breakup threshold anomaly is expected to be present in most of the target systems involving ^{6}Li, if other coupling effects (e.g., transfer, target inelastic excitation) are not so strong. The presence of the BTA in systems involving ^{6}Li can be attributed to the dominance of nuclear breakup couplings. It may be remarked that the situation can be quite different for the other weakly bound nuclei, e.g., ^{7}Li, where not only the coupling to the bound inelastic state can play a role but also the breakup couplings due to Coulomb part and different multipolarities may contribute in a different fashion. Recent experimental and theoretical works have suggested that the breakup is only a small component of the total reaction cross section for many systems. The neutron transfer mechanism is found to have a significant contribution in many of these cases. The good agreement of the CDCC calculations with the existing experimental data suggests that the transfer reactions not included in the present calculations are indeed of great interest for the present system and their influence needs to be explored. It may be conjectured that, while transfer processes could be of more importance for the studies related to fusion enhancement/suppression, the elastic scattering process is more influenced by the coupling to breakup mechanism because of its long distance behavior.

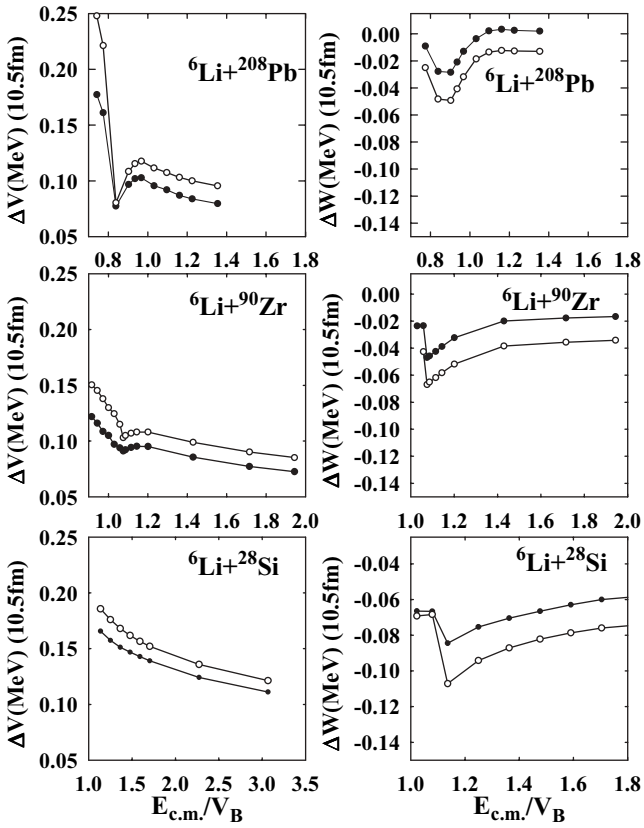

FIG. 9. Real and imaginary breakup polarization potentials due to nuclear+Coulomb coupling (solid circles) and nuclear coupling (empty circles) for the ^{6}Li + ^{208}Pb,^{6} Li + ^{90}Zr, and ^{6}Li + ^{28}Si systems, calculated in CDCC framework.

VIII. CONCLUSIONS

We have performed measurements for $^{6}Li + ^{90}Zr$ elastic scattering well below, near, and above barrier energies in a wide angular range. The results were analyzed with phenomenological optical potentials as well as with the microscopically generated optical potential using the double folding calculations. The data are consistent with the presence of breakup threshold anomaly observed in weakly bound systems. The derived potentials at the radius of sensitivity are well described by the dispersion relations. CDCC calculations were performed and a good description of the elastic data at all energies was obtained. A large coupling due to the breakup channel is observed and it affects the elastic cross section significantly at the backward angles. To understand the role of ^{6}Li breakup coupling on different target nuclei we performed CDCC calculations for the $^{6}Li + ^{208}Pb$ and $^{6}Li + ^{28}Si$ systems. The calculations suggest that scattering with ^{6}Li is dominated by the nuclear breakup even for heavier targets and the resulting polarization potential arising due to breakup couplings shows a rise in its imaginary part at near barrier energies. This observation suggests that the BTA is likely to be present for all systems in reactions with ^{6}Li, provided breakup coupling effects are dominant. The other coupling effects (target inelastic due to strong deformation of target and transfer reactions) may lead to different behavior and need to be explored. More experimental data near/below barrier with a systematic study of the target mass dependence are necessary to resolve the issue of relative importance of the couplings to other channels compared to breakup of ^{6}Li projectile.

ACKNOWLEDGMENTS

The authors thank the BARC/TIFR Pelletron staff for excellent delivery of the beam. One of the authors (B.J.R.) thanks the Research Centre, Jülich, for providing the enriched ^{90}Zr target.

[1] G. R. Satchler, Phys. Rep. **199**, 147 (1991).
[2] C. Mahaux *et al*., Nucl. Phys. **A449**, 354 (1986).
[3] M. S. Hussein, P. R. S. Gomes, J. Lubian, and L. C. Chamon, Phys. Rev. C **73**, 044610 (2006).
[4] M. S. Hussein, P. R. S. Gomes, J. Lubian, and L. C. Chamon, Phys. Rev. C **76**, 019902(E) (2007).
[5] N. Kelley *et al*., Nucl. Phys. **A571**, 326 (1994).
[6] M. A. Tiede, D. E. Trcka, and K. W. Kemper, Phys. Rev. C **44**, 1698 (1991).
[7] A. M. M. Maciel *et al*., Phys. Rev. C **59**, 2103 (1999).
[8] A. Pakou *et al*., Phys. Lett. **B556**, 21 (2003).
[9] A. Pakou *et al*., Phys. Rev. Lett. **90**, 202701 (2003).
[10] A. Pakou *et al*., Phys. Rev. C **69**, 054602 (2004).
[11] P. R. S. Gomes *et al*., Phys. Rev. C **71**, 034608 (2005).
[12] J. O. F. Niello *et al*., Nucl. Phys. **A787**, 484c (2007).
[13] F. A. Souza *et al*., Phys. Rev. C **75**, 044601 (2007).
[14] M. Biswas *et al*., Nucl. Phys. **A802**, 67 (2008).
[15] C. Beck, N. Keeley, and A. Diaz-Torres, Phys. Rev. C **75**, 054605 (2007).
[16] J. M. Figueira *et al*., Phys. Rev. C **75**, 017602 (2007).
[17] A. Chatterjee, LAMPS: Linux Advanced Multiparameter System (2008), http://www.tifr.res.in/pell/lamps.html.
[18] I. J. Thompson, FRESCO (May 2007), version FRES 2.3.
[19] R. J. Puigh and K. W. Kemper, Nucl. Phys. **A313**, 363 (1979).
[20] H. Wojciechowski, N. B. J. Tannous, R. H. Davis, D. Stanley, M. Golin, and F. Petrovich, Phys. Rev. C **17**, 2126 (1978).
[21] G. R. Satchler and W. G. Love, Phys. Rep. **55**, 183 (1979).
[22] J. Cook, Comput. Phys. Commun. **25**, 125 (1982).
[23] K. H. Bray *et al*., Nucl. Phys. **89**, 35 (1972).
[24] H. D. Vries *et al*., At. Data Nucl. Data Tables **36**, 495 (1987).
[25] S. Kailas, Phys. Rev. C **41(6)**, 2943 (1990).
[26] I. J. Thompson, Comput. Phys. Rep. **7**, 167 (1988).
[27] K. I. Kubo and M. Hirata, Nucl. Phys. **A187**, 186 (1972).
[28] A. Kumar *et al*., Nucl. Phys. **A776**, 105 (2006).
[29] C. M. Perey and F. G. Perey, Phys. Rev. C **132**, 755 (1963).
[30] I. J. Thompson *et al*., Nucl. Phys. **A505**, 84 (1989).
[31] Y. Sakuragi, Phys. Rev. C **35**, 2161 (1987).